Soft Matter

REVIEW

View Article Online
View Journal | View Issue



Cite this: *Soft Matter*, 2021, **17**, 222

# Increasing complexity in small-angle X-ray and neutron scattering experiments: from biological membrane mimics to live cells

Enrico F. Semeraro, [ab] Lisa Marx, [ab] Moritz P. K. Frewein [abc] and Georg Pabst *[ab]

Received 29th November 2019,
Accepted 7th February 2020

DOI: 10.1039/c9sm02352f

rsc.li/soft-matter-journal

Small-angle X-ray and neutron scattering are well-established, non-invasive experimental techniques to interrogate global structural properties of biological membrane mimicking systems under physiologically relevant conditions. Recent developments, both in bottom-up sample preparation techniques for increasingly complex model systems, and in data analysis techniques have opened the path toward addressing long standing issues of biological membrane remodelling processes. These efforts also include emerging quantitative scattering studies on live cells, thus enabling a bridging of molecular to cellular length scales. Here, we review recent progress in devising compositional models for joint small-angle X-ray and neutron scattering studies on diverse membrane mimics – with a specific focus on membrane structural coupling to amphiphatic peptides and integral proteins – and live *Escherichia coli*. In particular, we outline the present state-of-the-art in small-angle scattering methods applied to complex membrane systems, highlighting how increasing system complexity must be followed by an advance in compositional modelling and data-analysis tools.



## 1 Introduction

X-ray scattering experiments on membranes date back to the 1930–1940ies, when Gundo Boehm, Francis O. Schmitt and coworkers analyzed the fine structure of nerve myelin.[1,2] Yet, as a first step, it was necessary to explore the physicochemical properties of membrane lipids, which form the structural matrix of cellular envelopes. Vittorio Luzzati and coworkers, using small-angle X-ray scattering (SAXS), described in seminal studies performed in the 1960s[3] most of the diverse mesophases of membrane lipids, well before the fluid mosaic model for the structure of biological membranes was conceived by Singer and Nicholson.[4]

The following steadily growing awareness for lipid-only membranes as valuable tools for studying diverse aspects of membrane physiology under chemically well-defined conditions, created the need to resolve details of internal membrane structure. Note that scattering techniques, unlike most other structure-sensitive techniques, do not require the use of bulky labels, which potentially influence the structural equilibrium. Instead, selective deuterium labelling combined with small-angle neutron scattering (SANS), first demonstrated in groundbreaking studies by Büldt and Zaccai,[5,6] is often used to enhance structural resolution.

Another way to enhance structural resolution is to work at reduced levels of sample hydration. Wiener and White used this approach, when introducing a joint analysis of SAXS/SANS data of highly aligned lipid multibilayers,[7,8] and likewise John Nagle and coworkers, when evolving an earlier reported theory to accurately describe the line-shape of the Bragg peaks of multilamellar vesicles (MLVs).[9] But partial dehydration of samples affects the chemical equilibrium of lipid bilayers, which in turn influences interactions with membrane active compounds such as peptides or drugs. For such issues, it is highly desirable to work at full hydration. This was resolved a few years later by developing an analysis, which also took diffuse scattering contributions into account,[10] enabling a detailed structural analysis of fully hydrated MLVs made up of either single lipid species or homogeneous lipid mixtures. Working at full levels of hydration may, however, also lead to the formation of unilamellar vesicles, *e.g.*, due to membrane surface charges. Also sample preparation techniques, such as extrusion or sonication are often used to prepare single-shelled vesicles with a specific size. For the analysis of SAXS/SANS data from such samples, different techniques were developed.[11,12] In particular, the achievements of Kučerka and coworkers, who advanced the joint SAXS/SANS analysis technique by Wiener and White to

[a] *University of Graz, Institute of Molecular Biosciences, Biophysics Division, NAWI Graz, 8010 Graz, Austria. E-mail: georg.pabst@uni-graz.at; Tel: +43 316 380 4989*
[b] *BioTechMed Graz, 8010 Graz, Austria*
[c] *Institut Laue-Langevin, 38000 Grenoble, France*

unilamellar vesicles by coupling the analysis to molecular dynamics simulations, need to be mentioned in this context.[13]

The observation of fluid domains in cholesterol-containing ternary lipid mixtures at the turn of the century[14] changed gears in biomembrane research. Besides providing the ability to study the physicochemical properties of the previously proposed membrane rafts,[15] these systems also created the need to resolve structural details of the coexisting domains to understand *e.g.* protein partitioning into specific domains based on hydrophobic matching.[16] While SANS and SAXS are in principle sensitive to this information, further developments in data analysis were required. Pencer *et al.*, were the first to demonstrate the detection of submicron sized domains by SANS and subsequently developed tools to analyze their shape and size (see, ref. 17, for review). Later, our laboratory developed a method to analyze SAXS data for coexisting domains in MLVs,[18,19] gaining access to their specific transbilayer structural features. Finally, the advent of protocols to fabricate lipid vesicles with transbilayer asymmetry[20] not only made it possible to study more realistic plasma membrane mimics, but again demanded an evolution of SAXS/SANS data analysis to detail their leaflet-specific structure, which was achieved recently by Eicher *et al.*[21] Thus, increasing the complexity of membrane mimics always caused an adaptation of the scattering analysis.

In addition to all these bottom-up approaches of increasing system complexity, several groups have started to work out the scattering contributions of natural systems, starting from the early work on nerve myelin[1,2] and red blood cells[22] (which were still studied under quite dehydrated conditions) to live cells such as bacteria.[23,24] This opens up new avenues to bridge the gap between studies on model membranes and cells using the same techniques, *i.e.* with comparable experimental windows. Research along these directions is spurred by the ease of accessing large-scale facilities hosting either a neutron or synchrotron source. This allows researchers to combine the power of H/D contrast variation of neutron scattering with an array of scattering experiments enabled by the high photon flux available at synchrotron sources,[25] culminating at single particle/cell experiments using X-ray free electron lasers.

Focusing mainly on the remodelling of membrane systems mediated by peptides and proteins, the present review provides a timeline from past toward future scattering experiments on membrane mimics and live cells biased by the authors' contributions and knowledge of the field. Besides providing a general overview of structural details, we will also discuss the ability of scattering techniques to provide insight on intrinsically stored elastic properties of membranes which are of relevance for the function of integral membrane proteins.

## 2 General aspects of contrast in small-angle scattering experiments

SAXS and SANS data can be analysed by using the same formalism. In both cases, the scattering intensity, $I(q)$, is proportional to the square of the scattering density contrast, which is the difference between the scattering length densities (SLDs), $\rho$, of the molecule of interest and the suspension medium, $I(q) \propto (\rho - \rho_{\mathrm{medium}})^2$. The quantity $\rho$ is expressed as:

$$\rho = N_{\mathrm{A}} v^{-1} \sum_i n_i b_i, \quad (1)$$

where $N_{\mathrm{A}}$ is the Avogadro number, $v$ is molar volume and $b_i$ and $n_i$ are the coherent scattering length and number of elements $i$ in a given molecule, respectively. Briefly, the main difference between SAXS and SANS originates from X-ray photons, which scatter from electrons, whereas neutrons directly interact with atomic nuclei. This feature is reflected by the scattering length: for X-ray scattering, $b$ is proportional to the number of electrons in an atom (except for wavelengths close to the absorption edge of an element); in contrast, in the case of neutrons, $b$ assumes specific values for each element, with no relation to the atomic number (see Table 1).

Table 1 Examples of coherent scattering lengths $b$ for both X-ray and neutron interactions[26,27]

| Element/isotope | $b_{\text{X-ray}}$ (fm) | $b_{\text{neutron}}$ (fm) |
|---|---|---|
| Hydrogen ($^1$H) | 2.82 | −3.74 |
| Deuterium ($^2$D) | 2.82 | 6.67 |
| Carbon ($^{12}$C) | 16.9 | 6.65 |
| Nitrogen ($^{14}$N) | 19.7 | 9.36 |
| Oxygen ($^{16}$O) | 22.5 | 5.80 |
| Phosphorous ($^{31}$P) | 42.3 | 5.13 |

The difference in contrast between hydrogen and deuterium or light and heavy water (Table 2) allows for the powerful tool of H/D contrast variation.[28] Contrast-variation SANS measurements are usually performed by varying the percentage of heavy water in the suspension medium and/or by selectively substituting hydrogen with deuterium atoms in the macromolecules within the samples.[29] With this approach, specific regions of the system can be contrast matched regarding their SLD values and hence their contributions to the scattering intensity can be tuned.

Even though contrast-matching is also possible for SAXS, SANS offers a much wider range of contrast variation, without the need to alter the chemical composition of the suspension medium. Nonetheless, it is good practice to always verify if heavy water or deuterated macromolecules are affecting the native microstructure, kinetics and dynamics of the system. For example, the exchange of $H_2O$ by $D_2O$ may lead to a clear shift of the melting transition of single component lipid bilayers.[30]

Table 2 Examples of X-ray and neutron SLDs for some typical lipids components and water

| Molecule | $\rho_{\text{X-ray}}$ ($\times 10^{-4}$ nm$^{-2}$) | $\rho_{\text{neutron}}$ ($\times 10^{-4}$ nm$^{-2}$) |
|---|---|---|
| $H_2O$ | 9.39 | −0.56 |
| $D_2O$ | 9.38 | 6.73 |
| Phosphatidylglycerol (PG) (head-group) | 15.1 | 2.47/3.19[a] |
| Phosphatidylethanolamine (PE) (head-group) | 16.1 | 2.55/2.98[a] |
| Palmitic acid | 8.12 | −0.03 |
| Deuterated palmitic acid | 8.12 | 6.64 |

[a] Effective SLD in the case of complete H/D exchange of weakly bound hydrogens in 100 wt% $D_2O$ (two for PG and one for PE).

# 3 Compositional modelling of membranes

Reconstruction of structural information from scattering intensities in general involves either the application of Fourier transformation techniques or real-space modelling.[31,32] Using the latter approach enables detailed structural investigations of complex lipid systems considering their molecular composition. This was particularly demonstrated for membranes with heterogeneities, such as domains or transbilayer asymmetry. Below, we briefly summarize recent developments in the field. For more detailed reviews on these aspects, see, *e.g.* ref. 33 and 34.

## 3.1 Homogenous membranes

Over the years, diverse models for the transbilayer structure of lipid membranes have been reported.[35–39] Currently, the most refined way of describing a lipid bilayer are the scattering length density profile (SDP)[13] or the continuous distribution models.[37] In both models the scattering contrast is characterized in terms of a composition-dependent lipid parsing using volume-filling probability distribution functions. Specifically, the lipid bilayer is parsed into several quasimolecular fragments and their spatial distribution along the bilayer normal is described with either Gaussian[13] or error functions,[37] respectively see (Fig. 1A). This procedure is aided by comparison to molecular dynamics (MD) simulations. This yields composition-specific structural models that require supplementary information, such as the molecular lipid volumes as input parameters.

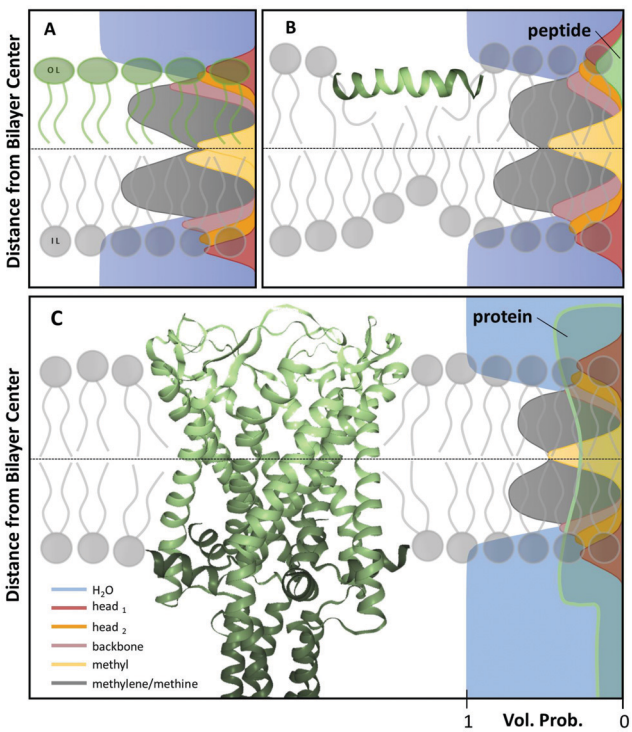


Fig. 1 Scattering length density models with distribution functions of Gaussian type for quasimolecular fragments of lipids in a bilayer (A) with asymmetric lipid composition, (B) including a surface-aligned amphipathic peptide (magainin 2; PDB code: 2MAG), or (C), an integral membrane protein (mechanosensitive channel of large conductance; PDB code: 2OAR).

The benefit of using volume distribution functions is the ability to jointly analyze SAXS and differently-contrasted SANS data, which increases structural fidelity. Typically reported parameters are the lateral area per lipid, the bilayer thickness and the length of the hydrocarbon chains. Moreover, this method can be readily extended to multilamellar vesicles,[40] which enables the analysis of bilayer interactions using the osmotic stress technique.[41] For a recent overview of published high-resolution structures of lipid membranes, see ref. 34.

## 3.2 Heterogeneous membranes

Heterogeneity in lipid-only membranes arises either from domains in symmetric bilayers, from leaflet-compositional asymmetry, or from a combination of both. The first type of lipid systems is a frequently applied model for gaining insight on membrane-rafts, whose proof of existence is still highly controversial in live cells.[42–44]

Lipid membranes composed of low-melting and high-melting lipids, as well as cholesterol, display coexisting liquid-ordered ($L_o$)/liquid-disorderd ($L_d$) domains, over a broad range of compositions and temperatures,[45] although it is important to discriminate between microscopic (*i.e.* micron-sized) and nanoscopic (few nanometers) domains. In the first case, scattering data can be modeled by a linear combination of homogeneous membranes (one representing $L_o$ and the other $L_d$ domains), while cross-correlations between $L_o$ and $L_d$ domains need to be considered for nanoscopic domains.[19] In both cases, modelling each lipid species individually would lead to an inordinate number of adjustable parameters. Therefore molecular averages of the individual lipid properties are utilized by defining a virtual hybrid molecule.[18] Using this approach, coexisting $L_o/L_d$ domains can be investigated *in situ*, gaining insight into structural details like cholesterol content.[19] In addition, information on domain size can be obtained. This is particularly important for nanoscopic domains that "escape" observation by light microscopy due to diffraction limitations. In-plane contrast is commonly much smaller than transverse contrast, but can be enhanced using SANS in combination with appropriate H/D variation schemes (Fig. 2). To investigate in-plane scattering contributions, transverse contrast has to be suppressed experimentally while enhancing lateral contrast.[12] This can be achieved by appropriate mixing of protiated and deuterated lipids, and adjusting the $H_2O/D_2O$ ratio of the surrounding aqueous solution. This way, nanoscopic domains with sizes as small as 13.6 nm were determined[46] Notably, highly ordered nanoscopic lipid domains enriched in cholesterol were also reported in binary mixtures with phosphatidylcholines using neutron diffraction on highly aligned multibilayers.[47,48] This supported the idea that $L_o$ and $L_d$ phases consist of inhomogenities due to fluctuations in cholesterol concentration within each domain (see, *e.g.*, ref. 33, for a recent review of this topic).

The second case of bilayer compositional complexity originates from an asymmetric distribution of lipids across the membrane leaflets. Interest in studying such systems arises from ubiquity of membrane asymmetry in biological cells.[50] Recent advances in developing protocols for fabrication of asymmetric large

 

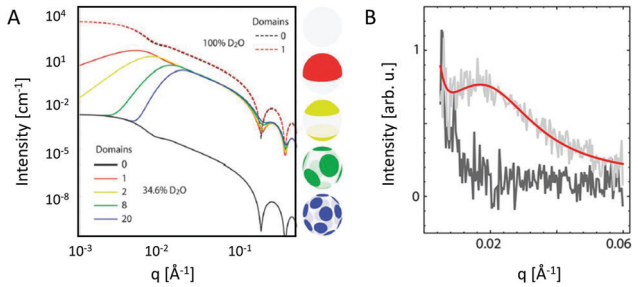


Fig. 2 Nanoscopic lipid domains investigated with SANS in combination with contrast variation. Panel A shows theoretical scattering curves for multidomain vesicles in either 100% $D_2O$ (dashed-lines) or 34.6% $D_2O$ (solid lines). Only the latter condition allows to differentiate between the different domains. Note that the transbilayer contrast is identical for all systems. Panel B shows the analysis of domain exhibiting vesicles (red line), or in a non phase separated (homogeneous) state (dark grey). Panel A: reproduced from ref. 33 with permission from The Royal Society of Chemistry, copyright 2015. Panel B: reproduced (adapted) from ref. 49 with permission from The American Chemical Society, copyright 2013.

unilamellar vesicles (aLUVs)[51–53] have paved the way for systematic studies of asymmetric membranes using an array of biophysical techniques, including SAXS and SANS. The unique advantage of neutron scattering in this regard is the ability to distinguish between the two leaflets, by placing chain deuterated lipids in one of the two monolayers. In this case, the compositional asymmetry is directly linked to a lift-off of the first minimum in the SANS pattern (Fig. 3). Further, it is possible to match the contrast of the aqueous solution with either leaflet to isolate the scattering of a single monolayer. The joint analysis of SAXS and SANS data then enables in-depth interrogation of leaflet-specific structural features, addressing *e.g.* transbilayer coupling in asymmetric bilayers.[21,51,54]

### 3.3 Inverted hexagonal phases – intrinsic lipid curvatures

Inverted hexagonal phases ($H_{II}$) are frequently formed by lipids of cone-like shape, such as *e.g.* phosphatidylethanolamines or glycolipids. Although inverted hexagonal structures have not been observed *in vivo* so far, membranes usually contain significant fractions of $H_{II}$-forming lipids. Thylakoid membranes, for example, were demonstrated to exhibit $H_{II}$ phases, if deprived of their protein content.[55] It has been hypothesized already in the 1980ies that the high content of non-bilayer forming lipids in membranes indicates mechanical coupling to protein function.[56] This can be rationalized on theoretical grounds in terms of the lateral pressure profile[57] or a line tension[58] that membranes exert on proteins.

A fundamental parameter, involved in both considerations is the intrinsic (or spontaneous) lipid curvature $C_0$, which describes the tendency of a lipid monolayer to curl away from a flat surface.[59] The lipid intrinsic curvature gives rise, *e.g.* to a stored elastic energy $E_0 = k_C C_0^2/2$, where $k_C$ is the monolayer bending rigidity. Importantly, $C_0$ must not be confused with the spontaneous bilayer curvature, which can be determined experimentally from tether-pulling experiments.[60]

The $H_{II}$ phase offers a valuable template for determining $C_0$ using SAXS.[61,62] Essentially, the problem condenses into finding the radius of the neutral plane $R_0$, since $C_0 = -R_0^{-1}$. It is reasonable to assume that $R_0$, which describes the plane where lipid bending and stretching modes are decoupled, occurs at the glycerol backbone.[63] One way to evaluate SAXS data of $H_{II}$ phases is reconstructing the electron density profile from the peak intensities *via* Fourier synthesis.[63] This readily yields the position of the lipid headgroups, from which $R_0$ can be estimated by adding a constant for the distance to the backbone determined from other experiments.

Compositional modelling of $H_{II}$ phases has the advantage of defining the position of $R_0$ within the model, thus increasing the reliability of $C_0$ determination. In this case, the lipid unit cell has a pie shape (Fig. 4A). For computational reasons it has been proven useful to parse the lipid molecule into different slabs, where $R_0$ is located in the center of the lipid backbone slab.[65]

Beside the headgroup size, $C_0$ is closely connected to the hydrocarbon chain composition (length and number of double bonds), which causes some disaturated phosphatidylethanolamines such as DMPE (dimyristoyl-phospatidylethanolamine) to have their $L_\alpha$-$H_{II}$ phase transition, $T_H$, at physiologically unrealistic temperatures. Experiments with $H_{II}$ phases are frequently performed with additional hydrophobic agents such as alkanes[61,66] or alkenes.[67] These agents do not only significantly lower $T_H$, but also reduce deformations of the cylinders by filling their interstices, thus yielding better estimates of the stress-free monolayer curvature. Interestingly, also ions significantly affect $C_0$. This can be understood by the reorientation of the lipid headgroups toward the aqueous phase,[68] which leads to a shift of $C_0$ to more negative values as observed for palmitoyl-oleoyl-phosphatidylethanolamine (POPE) (Table 3).

Lipids with approximately zero or positive $C_0$ do not form $H_{II}$ phases by themselves and have to be measured indirectly by mixing them with templates of $H_{II}$-forming (host-) lipids. Here, it is crucial to find the right way of accounting for the contributions of the guest lipids to the mixtures. As a zero order

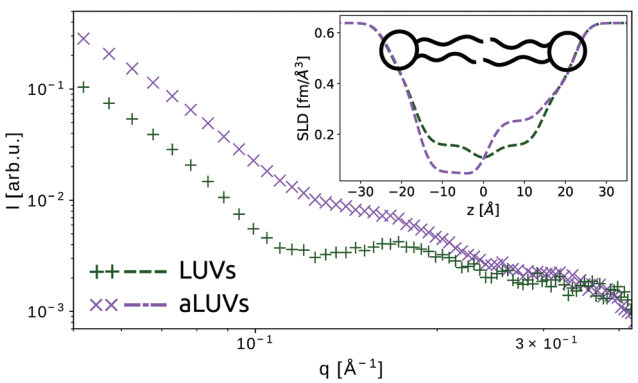


Fig. 3 SANS patterns of symmetric and asymmetric LUVs composed of chain-deuterated 1,2-dipalmitoyl-*sn-glycero*-3-phosphocholine (DPPC-d62) and 1-palmitoyl-2-oleoyl-*glycero*-3-phosphocholine (POPC) in 100% $D_2O$ (unpublished data recorded at the Institute Laue-Langevin, Grenoble, France, beamline D22). Symmetric LUVs show a distinct minimum around $q = 10^{-1}$ Å$^{-1}$, which is absent for aLUVs. The inset shows the corresponding trans-bilayer neutron-SLD profiles.

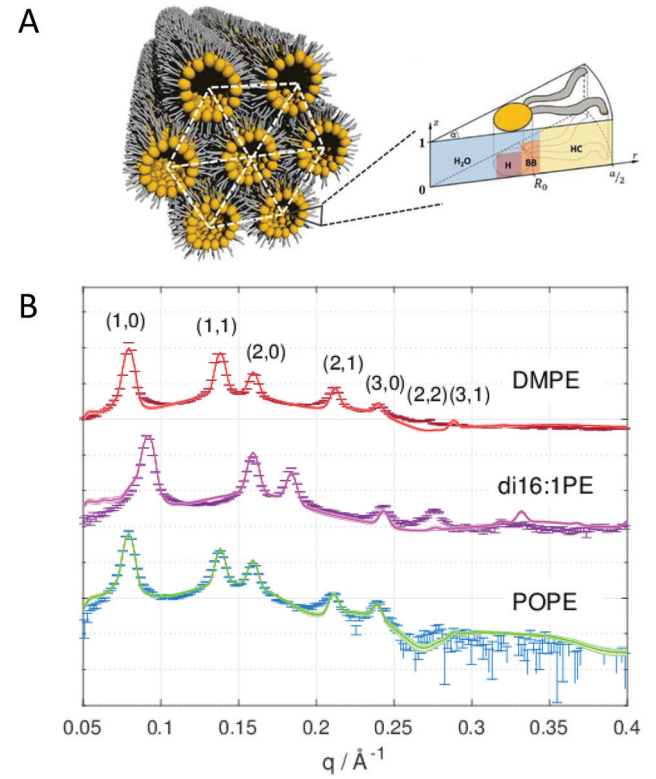


Fig. 4 Global analysis of $H_{II}$ phases. Panel A shows a cartoon of an inverted hexagonal phase and the compositional model of the lipid unit cell divided into $H_2O$, H (head), BB (backbone) and HC (hydrocarbon) slabs. Panel B shows successful fits to SAXS data of DMPE (dimyristoyl-phosphatidylethanolamine), di16:1PE (dipalmitoleoyl-phosphatidylethanolamine), and POPE (palmitoyl-oleoyl phosphatidylethanolamine) in the $H_{II}$ phase. Figures and data reproduced (adapted) from ref. 64 with permission of Springer, copyright 2009, and ref. 65 with permission from IUCr Journals, copyright 2019.

Table 3 Values for intrinsic curvatures $C_0$ of lipids in $H_2O$ or ionic buffer at 35 °C, gained from analysis of $H_{II}$ phases

| Lipid | $C_0$ (nm$^{-1}$) | Lipid | $C_0$ (nm$^{-1}$) |
|---|---|---|---|
| DMPE[a,d] | −0.314 ± 0.006[65] | Cholesterol[c] | −0.494 ± 0.013[63] |
| di16 : 1PE[a] | −0.382 ± 0.009[65] | DPPC[c] | +0.068 ± 0.032[63] |
| POPE[a] | −0.317 ± 0.007[65] | POPC[c] | −0.022 ± 0.010[63] |
| DOPE[a] | −0.409 ± 0.010[65] | DOPC[c] | −0.091 ± 0.008[63] |
| POPE[b,e] | −0.350 ± 0.007[69] | DLPE[c]+ | −0.22 ± 0.02[70] |
| DPPE[c,e] | −0.38 ± 0.19[70] | Lyso-PE[c,e] | +0.18 ± 0.12[69] |
| POPG[c,e] | −0.02 ± 0.03[69] | DOPG[c,e] | +0.03 ± 0.06[70] |

[a] Global analysis. [b] Fourier synthesis from peak intensities. [c] Linear extrapolation. [d] $T$ = 80 °C. [e] Prepared in NaPi-buffer (20 mM Na-phosphate, 130 mM NaCl, pH 7.4).

approximation, one can measure the total curvature from samples with varying host/guest lipid ratios and extrapolate linearly to 100% guest lipid content.[63] However, even approximating the lipids as rigid cones or cylinders can lead to a non-linear relationship for the total curvature, as for instance, if the headgroup sizes differ. In these cases, a more complex model is more appropriate to account also for lipid-specific interactions. We are currently exploring such approaches.

# 4 Membrane remodelling by proteins and peptides and *vice versa*

## 4.1 Amphipathic peptides

Interactions of amphiphatic peptides, such as *e.g.* antimicrobial peptides, with lipid model membranes have been widely studied with scattering techniques (see, *e.g.* ref. 71–73). Depending on the physicochemical properties of the peptides (size/length, polarity, charge, *etc.*) and the lipid membrane (thickness, charge, intrinsic curvature, elasticity, *etc.*), the peptides may either remain in a surface-aligned topology or insert at a given angle into the membrane.[69,74,75] In addition, aggregation of the peptides atop of the bilayer, or in the membrane-inserted topology in the case of pore formation, may lead to distinct membrane remodelling effects (see, *e.g.* ref. 76). Often these states are only transient or strongly fluctuate.

Peptides in the surface-aligned state typically cause significant membrane perturbation due to the need to bring the lipids of the opposing leaflet close to the hydrophobic surface of the peptide. This leads to the well-described effect of membrane thinning.[72] Fully inserted peptides, in turn, may not cause this effect, especially if the peptide length matches the hydrophobic thickness of the bilayer, although significant membrane softening may be induced.[77]

When peptides do not lead to an aggregation of LUVs (*e.g.* in the case of low peptide/lipid ratios) SAXS/SANS data can be analyzed in terms of transbilayer scattering length density models, similar to pure lipid membranes as discussed in Section 3. Specifically, peptides can be added to the volume probability distributions using either Gaussian or error functions (Fig. 1B). In the case of a transmembrane topology, only the latter one applies. However, adding the peptides requires appropriate removal of lipid contributions, hence, again, modelling largely benefits from coupling to MD simulations.[77,78] With this analysis, the peptide position in the bilayer can be determined with high accuracy by simultaneous statistical analysis of differently contrasted SAXS/SANS experiments.[78]

Using this approach we have most recently demonstrated distinct membrane effects for the surface-aligned antimicrobial peptides Magainin 2 (MG2a), PGLa and their equimolar mixture.[78] Specifically, by combining the scattering data analysis with MD simulations we found that PGLa, because of its lower mean hydrophobic moment, adsorbs slightly deeper into the headgroup region of POPE/palmitoyl-oleoyl-phosphatidylglycerol (POPG) mixtures than MG2a (Fig. 5). Moreover, we observed pronounced membrane thinning for the peptide mixtures at peptide/lipid ratios as low as 1/200, indicating an early onset of peptide heterodimer formation, consistent with MD simulations. The peptide heterodimers, which were found to be stabilized by salt bridges and hydrophobic forces, provide the nucleus of the well-known synergistic activity of MG2a and PGLa at elevated peptide concentrations.[69]

## 4.2 Integral proteins

Introducing bitopic or polytopic proteins adds even more degrees of freedom to the available parameter space for compositional

 

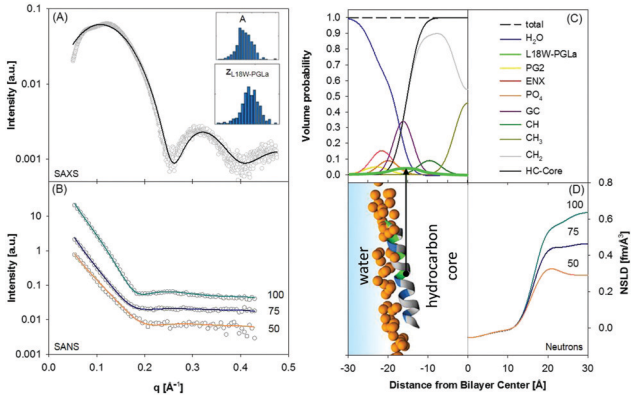


Fig. 5 Compositional modelling of surface-aligned PGLa in POPE/POPG (3 : 1 mol/mol) vesicles (peptide/lipid = 1/200). Panels (A) and (B) present SAXS and contrast variation SANS data, respectively. The inserts show histograms of the area per unit cell, $A_U$, and the position of the peptide in the bilayer, $z_P$, from 400 independent optimization runs. Panel (C) shows the volume probability distributions of the bilayer, and panel (D) displays a snapshot of an all-atom MD simulation (left) and neutron SLD profiles (right) for the different $D_2O$ concentrations. Figure reproduced from data reported in ref. 70.

models. These include vertical translation or tilting of the protein, but also its structural conformation and perturbation of the bilayer in the vicinity of the protein inclusion. Often the latter component is avoided by performing scattering experiments on membrane proteins reconstituted into detergent micelles (see, *e.g.* ref. 79–81). Naturally, the focus then is on protein structure and not on membrane remodeling by proteins. For a general review on the study of protein/lipid complexes using SANS, see ref. 82.

For proteins reconstituted into lipid membranes, essentially two approaches have been reported. None of them rely on proteoliposomes (*i.e.* proteins reconstituted into lipid vesicles), which suffer from ambiguities in transmembrane protein directionality (inside-out *vs.* outside-in). That is, detailed information on protein structure is challenged by its variable transmembrane orientations in proteoliposomes (see, *e.g.* ref. 83). The first strategy involves lipid nanodiscs.[84] In this case the orientations of the protein and the lipid disc are coupled (*i.e.* they diffuse/rotate in the aqueous phase as one entity). Scattering data has been described by a hybrid of a compositional model for the protein surrounding lipid bilayer and a bead-based model, frequently used for interpreting protein solution scattering.[85] The second approach for studying membrane inserted proteins has been developed for neutron reflectometry using bilayers sparsely tethered to a solid support (for review, see ref. 86). Briefly, the protein contribution to the scattering unit cell is considered by envelope functions determined by the proteins' cross-sectional areas along the transbilayer coordinate. When crystallographic information on the protein is available, its contribution can be considered as a rigid body. For proteins of unknown structure or highly flexible domains in the aqueous phase, model-independent parameterizations are also feasible. In particular, Hermite splines have proven to be a tractable route for representing the protein envelope (Fig. 1C). Upon combining the protein envelope with the lipid bilayer, it has been shown to be sufficient to adjust the positions of the lipid quasimolecular groups, while leaving the shape of their distribution unaltered.

**4.2.1 Effects of proteins on membrane structure.** As discussed above, most of the scattering studies reported on integral proteins focus on the low-resolution structure of the protein rather than on the effects of its inclusion on membrane structure (see, *e.g.* ref. 81). It is known however from complementary techniques that the lipid membrane may stretch or compress in the vicinity of an integral protein in order to match differences in the hydrophobic region.[16] Experimental evidence from scattering techniques on this aspect is scarce: this is mainly attributed to difficulties in data modelling. For example, the group of Lise Arleth reported a slight decrease (~1.5%) of membrane thickness in the case of bacteriorhodopsin-containing lipid nanodiscs.[85] Blasie and coworkers in turn found an asymmetric perturbation of a phosholipid bilayer containing the voltage-sensor domain of voltage-gated ion channels using neutron reflectometry on solid-supported systems.[87]

**4.2.2 Membrane-mediated effects on proteins: sorting into lipid domains.** Alternatively, properties of membrane lipids may also couple to the function of integral proteins. In general, lipid–protein interactions include a wide range of mechanisms such as specific binding sites,[88] annular lipids[89] or membrane-mediated effects, *e.g.* hydrophobic matching and membrane-tension related effects. Among the latter, the lateral pressure profile (LPP, see also Fig. 6)[57] can be used to estimate membrane-mediated effects on protein function. However, the LPP is hardly accessible by experiments and for its quantification one has to rely on mean-field theories or molecular dynamics simulations.[90] On the other hand, it has been shown[91] that for simple, rotationally-symmetric protein geometries the LPP is determined by a small number of parameters, *i.e.* intrinsic curvature, bending rigidity and

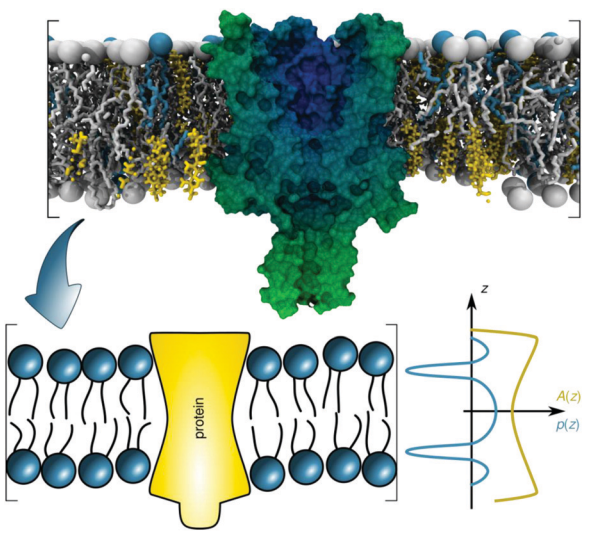


Fig. 6 Schematic overview of the lateral pressure profile $p(z)$ and its coupling to a membrane protein, where $z$ is the coordinate normal to the bilayer surface. For calculations, the complex shape of a membrane protein is transferred into a simple rotationally symmetric body with cross sectional area $A(z)$. Reproduced from ref. 92 with permission of The Royal Society of Chemistry, copyright 2016.

the position of the neutral plane $h$, all of which can be determined from scattering experiments.[18,41,63] Note that $h$ is here defined with respect to its distance from the center of the membrane.

The underlying theoretical framework enables calculating the contributions of lateral pressures to conformational changes of integral proteins (*e.g.* ion channels)[93] or preferential protein partitioning in a given lipid environment.[92] For example, we have derived the corresponding parameters from a ternary lipid mixture displaying a coexistence of liquid-ordered ($L_o$) and liquid-disordered ($L_d$) domains (Fig. 7A–C). $L_o$-domains exhibit, due to their increased concentration of cholesterol, a significantly more negative $C_0$ (see also Table 3). Further, due to the well-known membrane condensing effect of cholesterol, also $h$ and $k_C$ values are higher for $L_o$ (Fig. 7C). Using these parameters we calculated the work for moving a protein of specific shape into different lipid domains. Since parameters were derived for lipid monolayers, we were able to discriminate leaflet registered and antiregistered $L_o/L_d$ domains (*i.e.* upper/lower leaflet: $L_d/L_d$, $L_o/L_o$, $L_d/L_o$, $L_o/L_d$). Fig. 7D shows the results for five different protein shapes, where the preferred state is the one with the lowest strain energy. Clearly, the LPP of this specific lipid mixture drives proteins with concave geometries into $L_o$-domains, convex proteins into $L_d$-domains and cone-shaped ones into asymmetric membrane compartments (Fig. 7D). The effect is proportional to the protein radius, which means that the propensity for a certain state is increased for larger proteins.[92] Interestingly, asymmetric proteins prefer to be located within antiregistered (or asymmetric) domains. This suggests that integral proteins, most of which do have significant degrees of transmembrane asymmetry, energetically prefer an asymmetric lipid environment – alluding to a potential link to the abundance of asymmetry in natural membranes.

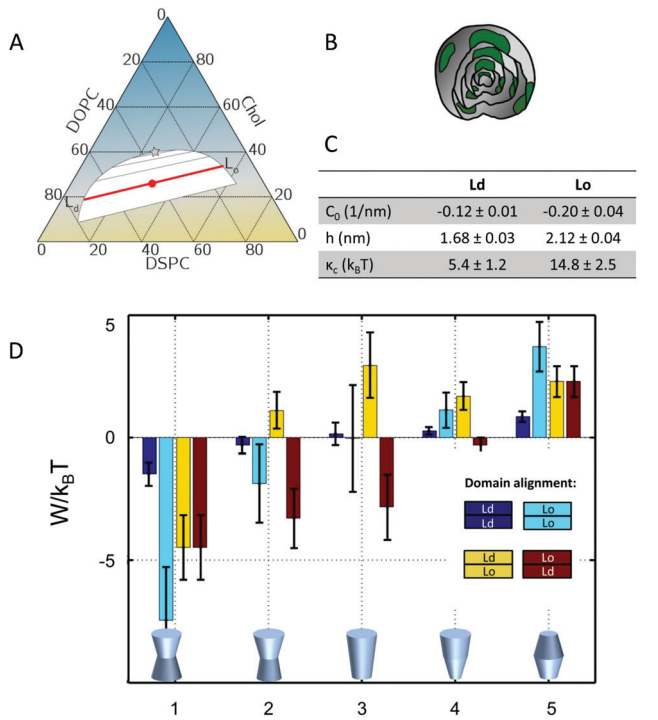


Fig. 7 Protein partitioning in a ternary mixture of dioleoyl-phosphatidylcholine (DOPC)/distearoyl-phosphatidylcholine (DSPC)/cholesterol (Chol) (0.42 : 0.37 : 0.21 mol/mol/mol). Panel A shows the compositional phase diagram (adapted from ref. 94 with permission of Elsevier, copyright 2007) and indicates the studied mixture as well its separation along the tie-line (red circle and red line). Panels B and C give a cartoon of the studied multilamellar vesicles containing domains and the corresponding structural/elastic parameters determined by SAXS, respectively. Panel D: stored lateral strain energy $W$ for proteins of different shapes in symmetric or asymmetric $L_o$ and $L_d$ domains. The overall preferred lipid environment for a given protein shape is given by the lowest $W/k_BT$-value. Reproduced from ref. 92 with permission of The Royal Society of Chemistry, copyright 2016.

## 5 Structural insights into live cells

Modelling scattering from live cells seems a taunting task in view of the vast complexity at various levels of structural hierarchy. Indeed, compared to lipid or lipid/protein systems, the degree of retrievable structural details decreases further with the increasing complexity of microorganisms. For example, SANS has been employed to investigate the periodicity of intracellular thylakoid membranes and its variations in connection to the photosynthetic processes in Gram-negative cyanobacteria.[95,96] More recently Nickels and coworkers[23] performed a nanoscale characterization of membrane heterogeneities of the Gram-positive bacterium *Bacillus subtilis*. The authors used chemical and genetical manipulations to contrast match all cellular components except for the membrane. This approach allowed them to demonstrate the existence of nanoscopic lipid domains in the bacteria's cell envelope.

Here, we focus on a multiscale (nm to μm) scattering model of *Escherichia coli*[24] – one of the most widely studied bacterial strains. The ultrastructure of bacteria is typically resolved by transmission electron microscopy (TEM).[97–101] However, TEM imaging is a massively invasive technique and requires fixation in combination with either staining,[97] or sample sectioning,[100] which might produce artifacts. The advantages of using high-resolution SAS are (i) the possibility to study live bacteria at variable sample conditions (pH, temperature, cosolutes, *etc.*); (ii) the exclusion of any artifacts originating from staining or labeling and (iii) the determination of structural features from ensemble averages from over $10^4$ to $10^{10}$ cell units from one single measurement. Nevertheless, TEM has been instrumental for constraining the multiscale scattering model of *E. coli*.[24] The model accounts for all cellular contributions by combining ultra-SAXS (USAXS)/SAXS and contrast-variation SANS. Note that USAXS extends the range of studied length scales to a few μm and a recent upgrade in synchrotron X-ray instrumentation for USAXS[102,103] allowed to fully exploit this technique for bacteria. To achieve this goal, several aspects need to be taken into account, which are summarized below.

*E. coli* are rod-shaped (length: 1.5–3 μm; diameter: 0.8–1 μm)[104] and have a cell wall composed of two membranes,[105] which envelope the cytoplasmic content. Specifically, the cytoplasm contains a long, folded DNA ring with associated proteins, which defines the nucleoid region; while the non-nucleoid volume includes ribosomes,

 

proteins, RNA, plasmids, *etc.* In both regions, the macromolecules are diffusing in an aqueous suspension of up to 1200 low-molecular-weight molecules (including nucleotides, aminoacids, alcohols, *etc.*) and ions.[106] Notably, DNA, tRNA and mRNA fill only 2% of the available volume, while ribosomes and proteins take up around 6–7 vol% and 13–16 vol%, respectively (values adapted from ref. 107). The average radius of gyration, $R_g$, from these cytoplasmic proteins is ~2 nm,[108] whereas ribosomes of *E. coli* are much bigger ($R_g$ = 8.8 nm) and have been well characterized in terms of their scattering form factor.[109]

The bacterial cell envelope of *E. coli* consists of two membranes enclosing the so-called periplasmic space. The periplasm has a thickness of about 20–30 nm[100] and hosts the peptidoglycan, or murein, layer, which is a net-like, stiff structure made up of long disaccharides chains that are covalently bridged by 4–5 amino acid sequences.[110] The lipid composition of the cytoplasmic membrane is dominated by phosphatidylethanolamine, phosphatidylglycerol and cardiolipin (about 85 : 5 : 10 molar ratio)[111] where the predominant hydrocarbon chains are C16:0 and C18:1 fatty acids.[112] The outer membrane is highly asymmetric, where the outer leaflet is almost exclusively composed of lipopolysaccharides and the inner leaflet consists of the same phospholipids found in the cytoplasmic membrane. The final structural components of *E. coli* to consider are flagella, which are protein-based helical tubes (length: 10–15 μm; diameter: ~20 nm)[113] that allow bacteria to perform their typical run-and-tumble dynamics.[114]

SANS is an indispensable tool to dissect the contributions of all these components making use of the so called scattering invariant, which is a measure of the overall sample contrast.[32] Briefly, the square-root of the scattering invariant as a function of $D_2O$ wt% shows the contribution of a given entity to the overall scattering signal. In the case of *E. coli*, the average contrast for phospholipids is "nullified" at about 11 wt% $D_2O$, while proteins and DNA are contrast-matched at 42 wt% and 65 wt% $D_2O$, respectively (Fig. 8A and B).

On the base of these estimations, the cytoplasm of *E. coli* was approximated by a prolate of homogeneous SLD, enveloped by several "shells" of different SLDs, describing the cell wall architecture including inner and outer membrane, the peptidoglycan layer and the periplasmic space (Fig. 8C). Note that scattering contributions from macromolecules (proteins, DNA, RNA, ribosomes, *etc.*) within the cell are negligible, *i.e.* they have poor contrast when compared to the average SLDs of their surroundings. In addition, the contribution from flagella was included as a smooth background *via* the asymptotic power law of the self-avoiding-walk polymer model,[115] *i.e.* a scattering intensity contribution proportional to $q^{-1.7}$.

The application of this scattering model provided quantitative measures of the bacterial cell envelope. For example, the average width of the periplasmic space was found to be 23 nm, which is in perfect agreement with the range of values (11–25 nm) reported from TEM.[98,100] Further, the periplasm was found to be much more dilute than observed from cryo-TEM using chemically fixed bacteria.[99] Indeed, results support more recent TEM data, which minimized sample alterations during preparation,[100] alluding again to potential artefacts

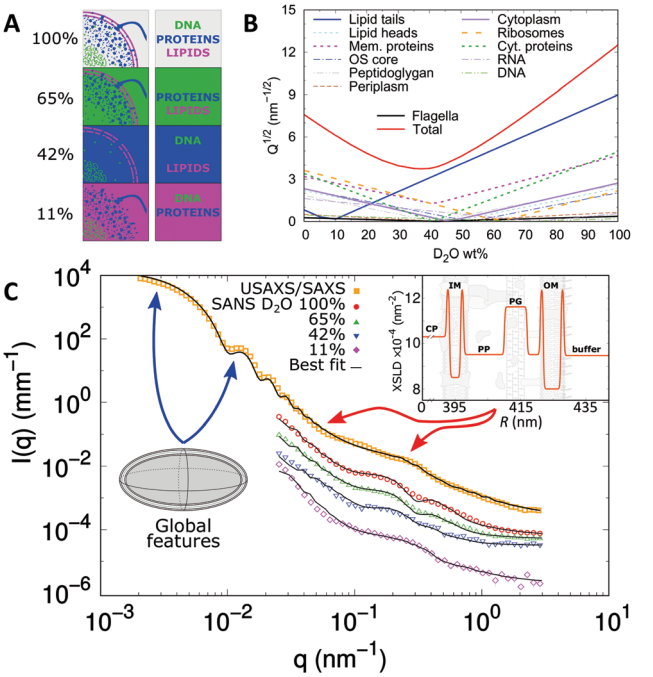


Fig. 8 Dissecting scattering from live *E. coli*. Panel A displays a schematic of contrast-matching cellular compartments at diverse $D_2O$ concentrations and panel B shows the corresponding scattering invariant estimated from the cellular composition. These include the main components of the cell-wall (left column) and cytoplasmic region (right column). Panel C shows the scattering intensities and fits of *E. coli* (SANS data have been re-scaled for visibility). The SLD profile of the cell-wall is composed of inner (IM) and outer membrane (OM), peptidoglycan layer (PG), cytoplasm (CP) and periplasm domain (PP). The arrows highlight the $q$-ranges where scattering features mostly refer to cell-body information (blue) or cell-wall characteristics (red). The inset shows the obtained X-ray SLD of the cell envelope. Reproduced (adapted) from ref. 24 with permission of IUCr Journals, copyright 2017.

introduced by labelling techniques. The distance between the peptidoglycan layer and the outer membrane is much more difficult to resolve with TEM. Semeraro *et al.*[24] reported a value of 11 nm for the center-to-center distance between the two layers, consistent with the length of the cylindrical Braun's lipoprotein Lpp-56, which connects the peptidoglycan and the outer membrane.[116] Finally, the inner membrane was observed to be slightly thinner (~4 nm) than the outer membrane (~6 nm),[24] which is most likely due to the larger headgroups of the outer LPS layer, although fine details, such as details of membrane asymmetry or headgroup structure are beyond experimental resolution.

## 6 Conclusions and outlook

Elastic scattering techniques (SAXS, SANS) provide a wealth of information on membrane structures and have a history of almost one hundred years. The benefits of these techniques definitely originate from the non-invasive nature and the ability to study systems under physiologically relevant conditions, without the need to resort to bulky labels. While most of its applications have been focused on homogeneous lipid-only membranes, the level of complexity of interrogated systems is

steadily increasing in order to match those studied by other, complementary techniques. These systems include domains, lipid asymmetry, as well as peptide–lipid or protein–lipid assemblies. Here, we have primarily focused on the latter systems. At the same time, possibly as a corollary to these efforts on bottom-up systems, researchers have commenced with quantitative scattering studies on live cells.

Admittedly, a broad application of quantitative elastic scattering on complex mimics or even live cells is challenged by the need of extensive data modelling. Specifically, scattering contributions from all sample components (*e.g.*, lipids, proteins, DNA) are convoluted within one signal. Hence, compositional modelling, *i.e.*, supplying the models with complementary information, limits the physically available/realistic parameter space, but also has to be carefully balanced against overparameterization. Thus, the overall large number of parameters requires application of an advanced global search optimization, including genetic algorithms, statistical data evaluation schemes, or machine learning methods, see *e.g.* ref. 19, 24, 65, 78, 86 and 117. Moreover, these latter techniques allow also simultaneous analysis of scattering data with complementary experiments or even optimization of the experimental setup, as reported recently for neutron reflectometry.[118]

Of particular interest for future studies are time-resolved experiments in combination with compositional modelling, exploiting the high photon fluxes available at synchrotron sources. For example, we are currently exploring the effect of antimicrobial peptides on live bacteria, which will yield insight into peptide targets and the evolution of peptide impact on bacteria on the nanoscopic to macroscopic length scales. Current limitations, such as averaging over dead and live cells, could be overcome by single-particle scattering measurements at X-ray free electron laser facilities. Note that SAXS and USAXS have already been used on qualitative grounds for screening of antibiotic effects on *E. coli*.[119,120]

Finally, efforts in sample preparation of bottom-up systems will allow to fabricate membrane mimics with controlled membrane asymmetry and integral protein directionality. This will boost the structural insight on membrane remodelling processes that can be gained. Hence, the future is bright in many aspects for elastic scattering techniques.

## Conflicts of interest

There are no conflicts to declare.

## Acknowledgements

This work was supported by the Austrian Science Funds (FWF), grant no. P30921.

## References

1 G. Boehm, *Kolloid-Z.*, 1933, **62**, 22–26.
2 F. O. Schmitt, R. S. Bear and K. J. Palmer, *J. Cell. Comp. Physiol.*, 1941, **18**, 31–42.
3 V. Luzzati, in *Biological membranes*, ed. D. Chapman, Academic Press, New York, 1968, pp. 71–123.
4 S. J. Singer and G. L. Nicholson, *Science*, 1972, **175**, 720–731.
5 G. Büldt, H. U. Gally, A. Seelig, J. Seelig and G. Zaccai, *Nature*, 1978, **271**, 182–184.
6 G. Zaccai, G. Büldt, A. Seelig and J. Seelig, *J. Mol. Biol.*, 1979, **134**, 693–706.
7 M. C. Wiener and S. H. White, *Biophys. J.*, 1991, **59**, 174–185.
8 M. C. Wiener and S. H. White, *Biophys. J.*, 1991, **59**, 162–173.
9 R. Zhang, R. M. Suter and J. F. Nagle, *Phys. Rev. E: Stat. Phys., Plasmas, Fluids, Relat. Interdiscip. Top.*, 1994, **50**, 5047–5059.
10 G. Pabst, M. Rappolt, H. Amenitsch and P. Laggner, *Phys. Rev. E: Stat. Phys., Plasmas, Fluids, Relat. Interdiscip. Top.*, 2000, **62**, 4000–4009.
11 O. Glatter, *J. Appl. Crystallogr.*, 1977, **10**, 415–421.
12 J. Pencer, S. Krueger, C. P. Adams and J. Katsaras, *J. Appl. Crystallogr.*, 2006, **39**, 293–303.
13 N. Kučerka, J. F. Nagle, J. N. Sachs, S. E. Feller, J. Pencer, A. Jackson and J. Katsaras, *Biophys. J.*, 2008, **95**, 2356–2367.
14 L. A. Bagatolli and E. Gratton, *Biophys. J.*, 2000, **79**, 434–447.
15 K. Simons and E. Ikonen, *Nature*, 1997, **387**, 569–572.
16 D. Marsh, *Biophys. J.*, 2008, **94**, 3996–4013.
17 J. Pencer, T. T. Mills, N. Kucerka, M. P. Nieh and J. Katsaras, *Methods Mol. Biol.*, 2007, **398**, 231–244.
18 P. Heftberger, B. Kollmitzer, A. A. Rieder, H. Amenitsch and G. Pabst, *Biophys. J.*, 2015, **108**, 854–862.
19 M. Belička, A. Weitzer and G. Pabst, *Soft Matter*, 2017, **13**, 1823–1833.
20 H. T. Cheng, Megha and E. London, *J. Biol. Chem.*, 2009, **284**, 6079–6092.
21 B. Eicher, F. A. Heberle, D. Marquardt, G. N. Rechberger, J. Katsaras and G. Pabst, *J. Appl. Crystallogr.*, 2017, **50**, 419–429.
22 L. McCaughan and S. Krimm, *Science*, 1980, **207**, 1481–1483.
23 J. D. Nickels, S. Chatterjee, C. B. Stanley, S. Qian, X. Cheng, D. A. A. Myles, R. F. Standaert, J. G. Elkins and J. Katsaras, *PLoS Biol.*, 2017, **15**, e2002214.
24 E. F. Semeraro, J. M. Devos, L. Porcar, V. T. Forsyth and T. Narayanan, *IUCrJ*, 2017, **4**, 751–757.
25 T. Narayanan and O. Konovalov, *Materials*, 2020, **13**, 752.
26 *X-ray Data Booklet*, ed. A. C. Thompson, Lawrence Berkeley National Laboratory, Berkeley, 3rd edn, 2009.
27 *Neutron Data Booklet*, ed. A.-J. Dianoux and G. Lander, Institut Laue-Langevin, Grenoble, 2nd edn, 2003.
28 P. Schurtenberger, in *Neutrons, X-rays and light: Scattering methods applied to soft condensed matter*, ed. P. Lindner and T. Zemb, Norh-Holland Elsevier, Amsterdam, 2002, ch. 7.
29 E. Mahieu and F. Gabel, *Acta Crystallogr., Sect. D: Struct. Biol.*, 2018, **74**, 715–726.
30 M. A. Kiselev and D. Lombardo, *Biochim. Biophys. Acta, Gen. Subj.*, 2017, **1861**, 3700–3717.
31 B. E. Warren, *X-ray diffraction*, Dover Publications, New York, 1990.
32 O. Glatter, *Scattering Methods and Their Application in Colloid and Interface Science*, Elsevier, 1st edn, 2018.
33 D. Marquardt, F. A. Heberle, J. D. Nickels, G. Pabst and J. Katsaras, *Soft Matter*, 2015, **11**, 9055–9072.

 

34 F. A. Heberle and G. Pabst, *Biophys. Rev.*, 2017, **9**, 353–373.
35 J. F. Nagle and S. Tristram-Nagle, *Biochim. Biophys. Acta*, 2000, **1469**, 159–195.
36 G. Pabst, N. Kučerka, M.-P. Nieh, M. C. Rheinstädter and J. Katsaras, *Chem. Phys. Lipids*, 2010, **163**, 460–479.
37 P. Shekhar, H. Nanda, M. Lösche and F. Heinrich, *J. Appl. Phys.*, 2011, **110**, 102216.
38 F. A. Heberle, J. Pan, R. F. Standaert, P. Drazba, N. Kučerka and J. Katsaras, *Eur. Biophys. J.*, 2012, **41**, 875–890.
39 J. C. Fogarty, M. Arjunwadkar, S. A. Pandit and J. Pan, *Biochim. Biophys. Acta*, 2015, **1848**, 662–672.
40 P. Heftberger, B. Kollmitzer, F. A. Heberle, J. Pan, M. Rappolt, H. Amenitsch, N. Kučerka, J. Katsaras and G. Pabst, *J. Appl. Crystallogr.*, 2014, **47**, 173–180.
41 B. Kollmitzer, P. Heftberger, R. Podgornik, J. F. Nagle and G. Pabst, *Biophys. J.*, 2015, **108**, 2833–2842.
42 C. Eggeling, C. Ringemann, R. Medda, G. Schwarzmann, K. Sandhoff, S. Polyakova, V. N. Belov, B. Hein, C. von Middendorff, A. Schonle and S. W. Hell, *Nature*, 2009, **457**, 1159–1162.
43 M. L. Kraft, *Mol. Biol. Cell*, 2013, **24**, 2765–2768.
44 E. Sevcsik, M. Brameshuber, M. Fölser, J. Weghuber, A. Honigmann and G. J. Schütz, *Nat. Commun.*, 2015, **6**, 6969.
45 D. G. Ackerman and G. W. Feigenson, *Essays Biochem.*, 2015, **57**, 33–42.
46 F. A. Heberle, M. Doktorova, S. L. Goh, R. F. Standaert, J. Katsaras and G. W. Feigenson, *J. Am. Chem. Soc.*, 2013, **135**, 14932–14935.
47 C. L. Armstrong, D. Marquardt, H. Dies, N. Kučerka, Z. Yamani, T. A. Harroun, J. Katsaras, A.-C. Shi and M. C. Rheinstädter, *PLoS One*, 2013, **8**, e66162.
48 L. Toppozini, S. Meinhardt, C. L. Armstrong, Z. Yamani, N. Kučerka, F. Schmid and M. C. Rheinstädter, *Phys. Rev. Lett.*, 2014, **113**, 228101.
49 F. A. Heberle, R. S. Petruzielo, J. Pan, P. Drazba, N. KuKučerka, R. F. Standaert, G. W. Feigenson and J. Katsaras, *J. Am. Chem. Soc.*, 2013, **135**, 6853–6859.
50 J. M. Boon and B. D. Smith, *Med. Res. Rev.*, 2002, **22**, 251–281.
51 F. A. Heberle, D. Marquardt, M. Doktorova, B. Geier, R. F. Standaert, P. Heftberger, B. Kollmitzer, J. D. Nickels, R. A. Dick and G. W. Feigenson, *et al.*, *Langmuir*, 2016, **32**, 5195–5200.
52 M. Doktorova, F. A. Heberle, B. Eicher, R. F. Standaert, J. Katsaras, E. London, G. Pabst and D. Marquardt, *Nat. Protoc.*, 2018, **13**, 2086–2101.
53 M. Markones, C. Drechsler, M. Kaiser, L. Kalie, H. Heerklotz and S. Fiedler, *Langmuir*, 2018, **34**, 1999–2005.
54 B. Eicher, D. Marquardt, F. A. Heberle, I. Letofsky-Papst, G. N. Rechberger, M.-S. Appavou, J. Katsaras and G. Pabst, *Biophys. J.*, 2018, 146–157.
55 I. Simidjiev, S. Stoylova, H. Amenitsch, T. Javorfi, L. Mustardy, P. Laggner, A. Holzenburg and G. Garab, *Proc. Natl. Acad. Sci. U. S. A.*, 2000, **97**, 1473–1476.
56 S. M. Gruner, *Proc. Natl. Acad. Sci. U. S. A.*, 1985, **82**, 3665–3669.
57 R. S. Cantor, *J. Phys. Chem. B*, 1997, **101**, 1723–1725.
58 N. Dan and S. A. Safran, *Biophys. J.*, 1998, **75**, 1410–1414.
59 J. M. Seddon and R. H. Templer, in *Structure and dynamics of membranes*, ed. R. Lipowsky and E. Sackmann, North-Holland, Amsterdam, 1995, pp. 97–160.
60 A. Callan-Jones, B. Sorre and P. Bassereau, *Cold Spring Harbor Perspect. Biol.*, 2011, **3**, a004648.
61 R. P. Rand, N. L. Fuller, S. M. Gruner and V. A. Parsegian, *Biochemistry*, 1990, **29**, 76–87.
62 S. H. Alley, O. Ces, M. Barahona and R. H. Templer, *Chem. Phys. Lipids*, 2008, **154**, 64–67.
63 B. Kollmitzer, P. Heftberger, M. Rappolt and G. Pabst, *Soft Matter*, 2013, **9**, 10877–10884.
64 G. Tresset, *PMC Biophys.*, 2009, **2**, 3.
65 M. P. K. Frewein, M. Rumetshofer and G. Pabst, *J. Appl. Crystallogr.*, 2019, **52**, 403–414.
66 M. W. Tate and S. M. Gruner, *Biochemistry*, 1989, **28**, 4245–4253.
67 H. P. Vacklin, B. J. Khoo, K. H. Madan, J. M. Seddon and R. H. Templer, *Langmuir*, 2000, **16**, 4741–4748.
68 J. Seelig, P. M. Macdonald and P. G. Scherer, *Biochemistry*, 1987, **26**, 7535–7541.
69 R. Leber, M. Pachler, I. Kabelka, I. Svoboda, D. Enkoller, R. Vácha, K. Lohner and G. Pabst, *Biophys. J.*, 2018, **114**, 1945–1954.
70 M. Pachler, PhD thesis, TU Graz, Graz, 2019.
71 K. Lohner and E. J. Prenner, *Biochim. Biophys. Acta*, 1999, **1462**, 141–156.
72 H. W. Huang, *Biochim. Biophys. Acta*, 2006, **1758**, 1292–1302.
73 A. Kumagai, F. G. Dupuy, Z. Arsov, Y. Elhady, D. Moody, R. K. Ernst, B. Deslouches, R. C. Montelaro, Y. Peter Di and S. Tristram-Nagle, *Soft Matter*, 2019, **15**, 1860–1868.
74 B. Bechinger, *Curr. Opin. Colloid Interface Sci.*, 2009, **14**, 349–355.
75 E. S. Salnikov and B. Bechinger, *Biophys. J.*, 2011, **100**, 1473–1480.
76 W. C. Wimley and K. Hristova, *J. Membr. Biol.*, 2011, **239**, 27–34.
77 J. Pan, D. P. Tieleman, J. F. Nagle, N. Kucerka and S. Tristram-Nagle, *Biochim. Biophys. Acta*, 2009, **1788**, 1387–1397.
78 M. Pachler, I. Kabelka, M.-S. Appavou, K. Lohner, R. Vácha and G. Pabst, *Biophys. J.*, 2019, **117**, 1858–1869.
79 A. Berthaud, J. Manzi, J. Pérez and S. Mangenot, *J. Am. Chem. Soc.*, 2012, **134**, 10080–10088.
80 A. Calcutta, C. M. Jessen, M. A. Behrens, C. L. P. Oliveira, M. L. Renart, J. M. González-Ros, D. E. Otzen, J. S. Pedersen, A. Malmendal and N. C. Nielsen, *Biochim. Biophys. Acta*, 2012, **1818**, 2290–2301.
81 C. Breyton, F. Gabel, M. Lethier, A. Flayhan, G. Durand, J.-M. Jault, C. Juillan-Binard, L. Imbert, M. Moulin, S. Ravaud, M. Härtlein and C. Ebel, *Eur. Phys. J. E: Soft Matter Biol. Phys.*, 2013, **36**, 71.
82 L. A. Clifton, C. Neylon and J. H. Lakey, *Methods Mol. Biol.*, 2013, **974**, 119–150.
83 K. A. Rubinson, C. Pokalsky, S. Krueger and L. J. Prochaska, *Protein J.*, 2013, **32**, 27–38.
84 M. A. Schuler, I. G. Denisov and S. G. Sligar, in *Lipid-protein Interactions*, ed. J. H. Kleinschmidt, Humana Press and Springer, New York, 2013, pp. 415–433.

85 S. A. R. Kynde, N. Skar-Gislinge, M. C. Pedersen, S. R. Midtgaard, J. B. Simonsen, R. Schweins, K. Mortensen and L. Arleth, *Acta Crystallogr., Sect. D: Struct. Biol.*, 2014, **70**, 371–383.
86 F. Heinrich and M. Lösche, *Biochim. Biophys. Acta*, 2014, **1838**, 2341–2349.
87 S. Gupta, J. A. Dura, J. A. Freites, D. J. Tobias and J. K. Blasie, *Langmuir*, 2012, **28**, 10504–10520.
88 Y. D. Paila, S. Tiwari and A. Chattopadhyay, *Biochim. Biophys. Acta*, 2009, **1788**, 295–302.
89 A. G. Lee, *Biochim. Biophys. Acta*, 2004, **1666**, 62–87.
90 O. H. Ollila and I. Vattulainen, in *Molecular Simulations and Biomembranes*, ed. M. S. P. Sansom and P. C. Biggin, RSC Publishing, London, UK, 2010, pp. 26–55.
91 R. S. Cantor, *Chem. Phys. Lipids*, 1999, **101**, 45–56.
92 M. Frewein, B. Kollmitzer, P. Heftberger and G. Pabst, *Soft Matter*, 2016, **12**, 3189–3195.
93 G. Pabst, S. L. Grage, S. Danner-Pongratz, W. Jing, A. S. Ulrich, A. Watts, K. Lohner and A. Hickel, *Biophys. J.*, 2008, **95**, 5779–5788.
94 J. Zhao, J. Wu, H. Shao, F. Kong, N. Jain, G. Hunt and G. Feigenson, *Biochim. Biophys. Acta*, 2007, **1768**, 2777–2786.
95 M. Liberton, L. E. Page, W. B. O'Dell, H. O'Neill, E. Mamontov, V. S. Urban and H. B. Pakrasi, *J. Biol. Chem.*, 2013, **288**, 3632–3640.
96 R. Ünnep, G. Nagy, M. Markó and G. Garab, *Plant Physiol. Biochem.*, 2014, **81**, 197–207.
97 J. A. Hobot, E. Carlemalm, W. Villiger and E. Kellenberger, *J. Bacteriol.*, 1984, **160**, 143–152.
98 L. L. Graham, T. J. Beveridge and N. Nanninga, *Trends Biochem. Sci.*, 1991, **16**, 328–329.
99 T. J. Beveridge, *J. Bacteriol.*, 1999, **181**, 4725–4733.
100 V. R. F. Matias, A. Al-amoudi, J. Dubochet and T. J. Beveridge, *J. Bacteriol.*, 2003, **185**, 6112–6118.
101 J. Milne and S. Subramaniam, *Nat. Rev. Microbiol.*, 2009, **7**, 666.
102 T. Narayanan, H. Wacklin, O. Konovalov and R. Lund, *Crystallogr. Rev.*, 2017, 160–226.
103 T. Narayanan, M. Sztucki, P. van Vaerenbergh, J. Léonardon, J. Gorini, L. Claustre, F. Sever, J. Morse and P. Boesecke, *J. Appl. Crystallogr.*, 2018, **51**, 1–14.
104 A.-C. Chien, N. S. Hill and P. A. Levin, *Curr. Biol.*, 2012, **22**, R340–R349.
105 T. J. Silhavy, D. Kahne and S. Walker, *Cold Spring Harbor Perspect. Biol.*, 2010, **2**, a000414.
106 R. P. Maharjan and T. Ferenci, *Anal. Biochem.*, 2003, **313**, 145–154.
107 *Escherichia coli and Salmonella typhimurium - Cellular and Molecular Biology*, ed. F. C. Neidhardt, American Society for Microbiology, Washington, DC, 1987.
108 S. B. Zimmerman and S. O. Trach, *J. Mol. Biol.*, 1991, **222**, 599–620.
109 D. Lebedev, A. Paleskava, A. Shvetcov, M. Polyakova, V. Isaev-Ivanov and A. L. Konevega, Time-resolved structural rearrangements of translocating ribosome: Experimental report LS 2406 (ESRF).
110 L. Gan, S. Chen and G. J. Jensen, *Proc. Natl. Acad. Sci. U. S. A.*, 2008, **105**, 18953–18957.
111 K. Lohner, E. Sevcsik and G. Pabst, *Liposome-Based Biomembrane Mimetic Systems: Implications for Lipid-Peptide Interactions*, 2008.
112 A. J. de Siervo, *J. Bacteriol.*, 1969, **100**, 1342–1349.
113 I. Yamashita, K. Hasegawa, H. Suzuki, F. Vonderviszt, Y. Mimori-Kiyosue and K. Namba, *Nat. Struct. Biol.*, 1998, **5**, 125–132.
114 L. Turner, R. Zhang, N. C. Darnton and H. C. Berg, *J. Bacteriol.*, 2010, **192**, 3259–3267.
115 P. Schurtenberger, in *Neutrons, X-rays and light: Scattering methods applied to soft condensed matter*, ed. P. Lindner and T. Zemb, Norh-Holland Elsevier, Amsterdam, 2002, ch. 11.
116 W. Shu, J. Liu, H. Ji and M. Lu, *J. Mol. Biol.*, 2000, **299**, 1101–1112.
117 D. Franke, C. M. Jeffries and D. I. Svergun, *Biophys. J.*, 2018, **114**, 2485–2492.
118 B. W. Treece, P. A. Kienzle, D. P. Hoogerheide, C. F. Majkrzak, M. Lösche and F. Heinrich, *J. Appl. Crystallogr.*, 2019, **52**, 47–59.
119 A. R. von Gundlach, V. M. Garamus, T. Gorniak, H. A. Davies, M. Reischl, R. Mikut, K. Hilpert and A. Rosenhahn, *Biochim. Biophys. Acta*, 2015, **1858**, 918–925.
120 A. R. von Gundlach, V. M. Garamus, T. M. Willey, J. Ilavsky, K. Hilpert and A. Rosenhahn, *J. Appl. Crystallogr.*, 2016, **49**, 2210–2216.

 